Chemical Physics Letters 841 (2024) 141178

Contents lists available at ScienceDirect

Chemical Physics Letters

journal homepage: www.elsevier.com/locate/cplett

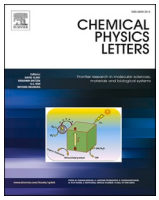

Single-walled carbon nanotube synthesis with RuRhPdIrPt high entropy alloy catalysts

Shu Matsuoka [a], Kamal Prasad Sharma [b], Takahiro Saida [a,b], Kohei Kusada [c,d], Hiroshi Kitagawa [c], Takahiro Maruyama [a,b,*]

[a] Department of Applied Chemistry, Meijo University, Tempaku-ku, Nagoya 468-8502, Japan
[b] Nanomaterial Research Center, Meijo University, Tempaku-ku, Nagoya 468-8502, Japan
[c] Division of Chemistry, Graduate School of Science, Kyoto University, Sakyo-ku, Kyoto 606-8502, Japan
[d] The Hakubi Center for Advanced Research, Kyoto University, Sakyo-ku, Kyoto 606-8502, Japan

ARTICLE INFO

Keywords:
Carbon nanotube
High Entropy Alloy
CVD
Catalyst
Raman

ABSTRACT

Using high-entropy alloy nanoparticles (HEA NPs) composed of five platinum-group metals (5PGM), Ru, Rh, Pd, Ir, and Pt, as catalysts, we succeeded in growing single-walled carbon nanotubes (SWCNTs) via chemical vapor deposition (CVD). After CVD growth with C_2H_2 feedstock at 750 ℃ for 10 min, high-density SWCNTs were grown from 5PGM HEA NPs. The diameters of most SWCNTs were in the range of 0.83–1.1 nm, exhibiting the growth of small-diameter SWCNTs. Compared with monometal PGM catalysts, the SWCNT yield with the 5PGM HEA NP catalysts was much higher and was compatible even with those with Fe and Co.

1. Introduction

Recently, high-entropy alloys (HEAs), which are solid solutions consisting of five or more elements in an approximately equal atomic ratio [1–3], have attracted tremendous attention in various fields because of their specific properties such as high hardness and strength and high thermal and chemical stabilities. In addition, compared to conventional monometals and binary alloys, HEAs exhibit unique surface and electronic structures because all surface atoms have different configurations with specific local electronic structures. Such a complex surface structure composed of random multi-element mixing contains diverse active sites for various catalytic reactions [4]. Notably, in the past few years, the catalytic properties of HEA nanoparticles (NPs) have been extensively investigated. Yao et al. reported that RuRhPdPtCe and RuRhIrCoNi HEA NPs showed high activity in NH_3 oxidation and NH_3 decomposition, respectively [5,6]. Loffler et al. observed that CrMnFeCoNi NPs exhibit high activity in oxygen reduction reaction (ORR) [7]. Recently, Kitagawa et al. successfully synthesized HEA NPs composed of platinum group metals (PGMs) [8–13], and observed that RuRhPdOsIrPt catalyzes ethanol oxidation with a 12-electron process [10]. However, despite their potential in catalytic applications, HEA NPs have never been used as catalysts for carbon nanotube (CNT) growth.

In this study, we attempted to grow single-walled CNTs (SWCNTs) using HEA NPs comprising five platinum group metals (5PGM; Rh, Ru, Pd, Ir, and Pt). To date, our group has reported the SWCNT growth using PGMs as catalysts and demonstrated that they act as effective catalysts [14–20]; we reported the SWCNT growth below 300 ℃ with a Rh catalyst [14], and observed that Ir and Pt are effective catalysts to grow small-diameter SWCNTs with diameters below 1.1 nm [14,18,19]. In particular, vertically aligned (VA-)SWCNTs with small diameters were grown with Ir catalysts [18,19]. The fact that VA-SWCNTs were obtained with sufficiently high-density growth indicates that Ir is a highly active catalyst for SWCNT growth. Considering that PGM HEA NPs often exhibit higher activity than monometal PGM catalysts in various reactions, HEA NPs composed of PGMs might act as highly active catalysts, even for SWCNT growth. Herein, we performed SWCNT growth by chemical vapor deposition (CVD) using a C_2H_2 feedstock with 5PGM NPs as the catalyst. Our results showed that the 5PGM HEA NPs demonstrated superior catalytic performance for the growth of small-diameter SWCNTs.

2. Experimental procedure

2.1. Synthesis of 5PGM HEA NPs

The synthesis of the 5PGM HEA NPs catalysts has been described

* Corresponding author at: Department of Applied Chemistry, Meijo University, Tempaku-ku, Nagoya 468-8502, Japan.
E-mail address: takamaru@meijo-u.ac.jp (T. Maruyama).

https://doi.org/10.1016/j.cplett.2024.141178
Received 7 December 2023; Received in revised form 2 March 2024; Accepted 4 March 2024
Available online 6 March 2024

previously [9]. Briefly, 5PGM HEA NPs were obtained by injecting a mixed aqueous solution of five metal precursors, $RuCl_3{\cdot}nH_2O$, $RhCl_3{\cdot}3H_2O$, $K_2[PdCl_4]$, $IrCl_4{\cdot}nH_2O$, and $K_2[PtCl_4]$, in an equimolar ratio (approximately 16.7 at%; each precursor concentration is 0.1 M) at 5.0 mL/min to a preheated 50 vol% of ethanol aqueous solution containing KOH at 5 mM pumped at 50.0 mL/min at 230 ℃ under 8.0 MPa using the flow reactor. Also, poly (N-vinyl-2-pyrrolidone) (PVP, K30) as a protecting agent was dissolved in the precursors' solution before injection. Ethanol acts as both a reducing agent and a solvent. The mixture was quickly cooled to room temperature through the chiller, and the ejected black solution was washed several times with a mixture of acetone, water, and ether to remove the excess PVP. Finally, a black powder was collected via centrifugation and vacuum drying at room temperature.

PGM HEA NPs were characterized using transmission electron microscope (TEM; JEM-ARM 200F, JEM-2100F, JEOL, Tokyo, Japan) at an accelerating voltage of 200 kV, where high-angle annular dark-field scanning TEM (HAADF-STEM) and annular bright field scanning TEM (ABF-STEM) coupled with energy-dispersive X-ray (EDX) spectroscopy were used. In addition, pair distribution function (PDF) was obtained from electron diffraction in TEM. For TEM observation, the dispersed 5PGM HEA NP solution was dropped onto TEM grids (HRC-C10 Cu100P, STEM, Tokyo, Japan), followed by drying at room temperature. Their structures and compositions were determined by X-ray diffraction (XRD; SmartLab, Rigaku, Tokyo, Japan) and X-ray photoelectron spectroscopy (XPS; JPS-9200, JEOL, Tokyo, Japan), respectively. A Mg K_α X-ray source was used for the XPS analysis. Using the XPS analysis, we also measured the valence band spectra of Ru, Pd, Ir, Pt, Fe, and Co to determine the d-band centers. In this analysis, we measured the Ru, Pd, Ir, and Pt particles deposited on SiO_2/Si substrates by the pulsed arc plasma deposition system (APD-2S, ADVANCE-RIKO, Yokohama, Japan). In the case of Fe and Co, XPS analysis was performed for Fe and Co thin films formed on SiO_2/Si substrates after Ar sputtering for 10 min to remove the surface oxides. In addition, XPS measurements were performed for the top of the valence band of the Au films to determine the Fermi level and evaluate the energy position of the d-band center with respect to the Fermi level.

2.2. SWCNT growth

For use as a catalyst for SWCNT growth, the 5PGM HEA NPs were dispersed in ethanol by the ultrasonic homogenizer (Sonifier SFX150, Branson, USA); then the dispersion liquid containing 5PGM HEA NPs were spin-coated on SiO_2/Si substrates. After heating at 400 ℃ in the air to remove PVP coating from 5PGM HEA NPs, the substrates were mounted in a reactor, and SWCNTs were grown in hot-wall CVD using C_2H_2 as feedstock with 5PGM HEA NPs as catalysts; SiO_2/Si substrates with the 5PGM HEA NPs were placed in a quartz tube inside an electric furnace (Fig. S1). The quartz tube was evacuated using a scroll pump and the base pressure was maintained below 5 Pa. During heating in the electric furnace, Ar/H_2 (5 % H_2) was supplied at a flow rate of 1000 sccm. After the furnace reached the desired temperature, the supply of Ar/H_2 was stopped and Ar/C_2H_2 (2.5 % C_2H_2) was used for SWCNT growth. In this experiment, the growth temperature and growth time were set at 700–850 ℃, and 10 min, respectively. The morphology of the SWCNTs was characterized using field-emission scanning electron microscopy (FE-SEM; SU-8010, Hitachi Ltd., Tokyo, Japan). To characterize the crystalline quality and SWCNT yield, the Raman spectra of the samples were measured using a Micro-Raman system (RAMANforce, Nanophoton, Osaka, Japan). The excitation wavelengths used for Raman measurements were 488, 532, 671, and 785 nm, where the detection area was about 1 μm. The SWCNTs were also characterized by TEM (JEM-2100F, JEOL). For TEM observations, SWCNTs grown on SiO_2/Si substrates were exfoliated from the substrates using polymethyl methacrylate (PMMA) films, which were formed by the drop casting method from PMMA/acetone solution. Then, the PMMA film containing SWCNTs was dissolved in a mixture of 10 % N, N-dimethylformamide, and acetone, followed by dispersion with the ultrasonic homogenizer (Sonifier SFX150, Branson, USA). Finally, the solution was dropped onto TEM grids (HRC-C10 Cu100P, STEM, Tokyo, Japan) and cleaned with acetone vapor to remove residual PMMA.

For reference, SWCNT growth were also performed with monometallic Ru, Pd, Ir, Pt, Fe, and Co NPs, which were prepared by pulsed arc plasma deposition in high vacuum. The particle size of each element was characterized by TEM (JEM-ARM 200F, JEM-2100F, JEOL) at an accelerating voltage of 200 kV. To characterize the particle sizes, we deposited each catalyst metal on the SiO_2 membrane TEM window grid (SO200-A40L, ALLIANCE Biosytems, Osaka, Japan). The typical particle size of each element was in the range of 0.5–3 nm (Fig. S2), which is suitable for SWCNT growth. For SWCNT growth, Ru, Pd, Ir, and Pt catalyst particles were deposited on SiO_2/Si substrates, and Fe and Co catalyst particles were deposited on Al_2O_3(20 nm)/SiO_2/Si/substrates; these are the common support layers for each catalyst metal to obtain high-yield SWCNTs. To compare the amount of each monometal catalyst on the substrate with that of 5PGM HEA NPs, we performed XPS measurement for both monometal catalysts and 5PGM HEA NPs, where XPS analysis for the latter was performed after removing PVP by heating in air. The relative peak intensity of each constituent element in XPS spectra for 5PGM HEA NPs on the SiO_2/Si substrate was less than 1/5 of each monometal catalyst particle deposited by the pulsed arc plasma method (Fig. S3). This indicates that the amount of 5PGM HEA NPs on the substrate was smaller than that of each monometal catalyst.

3. Results and discussion

3.1. Characterization of 5PGM HEA NPs

Fig. 1(a) shows the ABF-STEM images of the 5PGM HEA NPs; black particles are observed. The high-resolution TEM (HRTEM) image shows lattice fringes with a spacing of 0.223 nm (Fig. 1(b)), confirming the highly crystalline character of the NPs. Fig. 1(c) shows the size distribution of the NPs. The sizes of NPs are in the range of 0.8–7.6 nm with an average size of 3.12 nm; the sizes are predominantly below 4 nm. Considering that the amount of 5PGM HEA NPs on the substrate was not higher than those of monometal catalysts deposited by the pulsed arc plasma method, the density of 5PGM HEA NPs would be smaller than those of monometal catalyst particles because the sizes of 5PGM HEA NPs were slightly larger than those of monometal catalysts. The XRD pattern shows that the 5PGM HEA NPs have a single-phase face-centered cubic (fcc) structure with a lattice parameter of a = 0.386 nm (Fig. 2). This corresponds to an interplanar spacing of 0.223 nm in the (1 1 1) plane of the fcc structure, which is consistent with the HRTEM image shown in Fig. 1(b). Fig. 3 (a)-(f) shows the EDX maps of Ru, Rh, Pd, Ir, Pt, and their mixtures for 5PGM HEA NPs. These maps show that each element is homogenously distributed throughout the NPs. The STEM-EDX point analysis showed that the composition ratio of each element was similar in the 5PGM HEA NPs (Fig. 3 (g) and (h)). We also investigated the composition of the 5PGM HEA NPs using XPS. Fig. 4 (a)–(e) shows the core-level XPS spectra of Ru, Rh, Pd, Ir, and Pt in the 5PGM HEA NPs. The XPS core-level spectrum of each element was fitted to one component that had binding energy on the red line with its bulk metal. This indicates that all the elements are in the metallic state, as reported in a previous study [10]. Considering the relative sensitivity factor (RSF) of each element in the XPS system, the composition ratio of each element was estimated from the peak intensity. The composition ratios obtained are shown in Fig. 4(f). The atomic percentages of each element determined by XPS are almost the same among the 5PGM elements. From the TEM, XRD, and EDX characterizations, we concluded that the 5PGM HEA NPs were solid solutions, where the composition ratio of each constituent element was almost equal, and each constituent element was homogenously distributed.

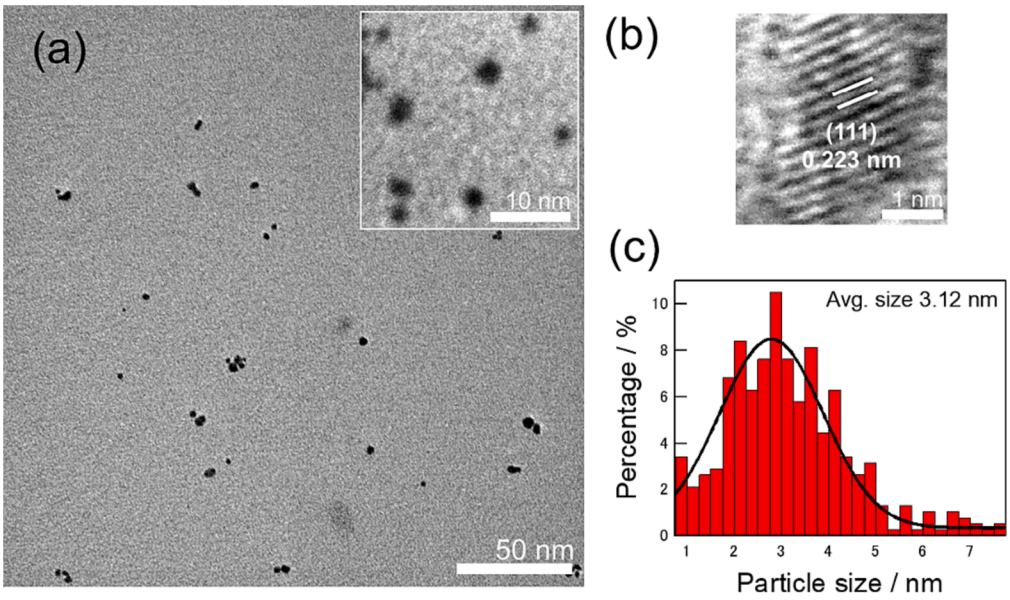

Fig. 1. (a) TEM images and (b) High-resolution TEM image of 5PGM HEA NPs. Black particles in (a) are 5PGM HEA NPs. (c) Particle size distribution of 5PGM HEA NPs. The inset of (a) shows ABF-STEM image of 5PGM HEA NPs.

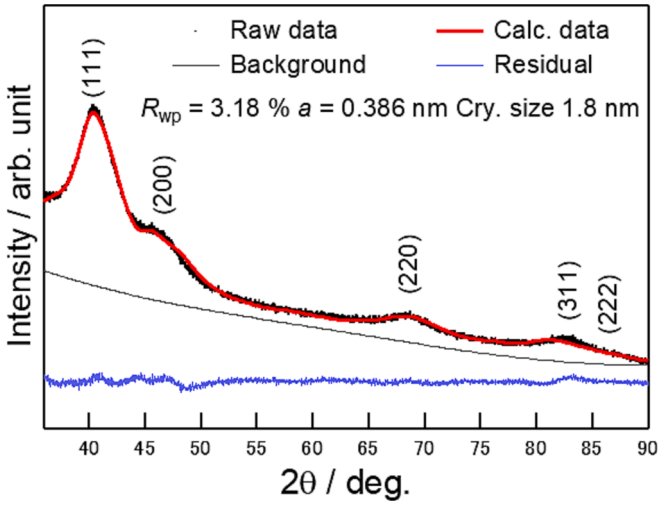

Fig. 2. XRD pattern of 5PGM HEA NPs.

3.2. SWCNT growth

Using the 5PGM HEA NPs as catalysts, we grew SWCNTs using Ar/C_2H_2 as the feedstock. Fig. 5(a) shows the Raman spectra of SWCNTs grown at 700 –850 ℃. The flow rates of Ar/C_2H_2 were optimized for each growth temperature (50, 300, 600, and 900 sccm for 700 ℃, 750 ℃, 800 ℃, and 850 ℃, respectively). In all spectra, G-band peaks appear at approximately 1585 cm^{-1}, and radial breathing mode (RBM) peaks are observed in the range of 130–310 cm^{-1}. This indicates that SWCNTs were grown from the 5PGM HEA NP catalysts in this temperature range. D-band peaks are also observed at ~ 1350 cm^{-1}; however, their intensities are lower than those of the G-band for each growth temperature. Considering that the D-band peak was derived from defects in the graphene lattice or amorphous carbon [21], the G/D ratio corresponded to the crystalline quality of the grown SWCNTs. At 750 ℃, the G/D ratio reached its maximum (4.6), where the intensities of the G band and RBM peaks became the strongest. This indicates that the crystalline quality of SWCNTs was best at 750 ℃, where the SWCNT yield was the highest. The G/D ratio at 750 ℃ was compatible with those grown from monometal PGM NPs [14–20], exhibiting comparatively good quality of SWCNTs grown with 5PGM HEA NP catalysts.

To investigate the structural property of SWCNTs grown from 5PGM HEA NPs, we performed Raman spectroscopy for SWCNTs grown at 750 ℃ using lasers with four excitation wavelengths because the RBM peak intensities are significantly enhanced under the resonant condition. Fig. 5(b) shows the Raman spectra of SWCNTs grown at 750 ℃ under the optimal flow rate of Ar/C_2H_2 (300 sccm). Irrespective of the excitation wavelength, both RBM and G-band peaks are observed. The RBM peaks are observed in the range of 134–298 cm^{-1} and mainly distributed at 222–298 cm^{-1}. Using the relationship between the SWCNT diameter (nm) and wavenumber of an RBM peak (cm^{-1}), ω_{RBM} (cm^{-1}) = 248/d (nm) [22], most of the grown SWCNTs had diameters of 0.83–1.1 nm. Fig. 6 shows the SEM and TEM images of the SWCNTs grown from the 5PGM HEA NPs. The SEM image shows that web-like SWCNTs are grown from 5PGM HEA NPs, and the lengths of most SWCNTs are longer than 1 μm (Fig. 6(a)). The TEM image shows that SWCNTs are grown from the 5PGM HEA NPs, and they formed bundles (Fig. 6(b)). The diameters of the SWCNTs are ~ 1 nm, as shown in the inset of Fig. 6(b), although they showed wavy structures induced by the electron irradiation damage. Their diameters are consistent with those of the RBM peaks estimated from Raman spectra. The existence of amorphous carbon was not confirmed in SEM and TEM observations, suggesting that D-band peak in Raman spectrum was mainly derived from the defects in SWCNTs.

To investigate the robustness of the 5PGM HEA NP catalysts, we performed STEM-EDX mapping of the 5PGM HEA NPs after SWCNT growth. Fig. 7 (a)-(f) shows the STEM- HAADF images and corresponding EDX maps of Ru, Rh, Pd, Ir, and Pt. These maps show that, after SWCNT growth, each element is homogeneously distributed throughout the NPs, confirming the robustness of the 5PGM HEA NPs through SWCNT growth. Considering that SWCNTs are generally grown from catalyst particles with diameters less than 3 nm [23], we also performed STEM-EDX point analysis for 5PGM HEA NPs with the smaller diameter. Fig. 7 (g) shows the STEM-HAADF image of 5PGM HEA NPs with diameters less than 6 nm after SWCNT growth and the composition ratio obtained for a red point in (g) using STEM-EDX point analysis is shown in Fig. 7(h). The composition ratio of each element was not significantly different, indicating that phase separation did not occur in 5PGM HEA NPs during SWCNT growth.

We also performed XRD and PDF analysis for 5PGM HEA NPs after

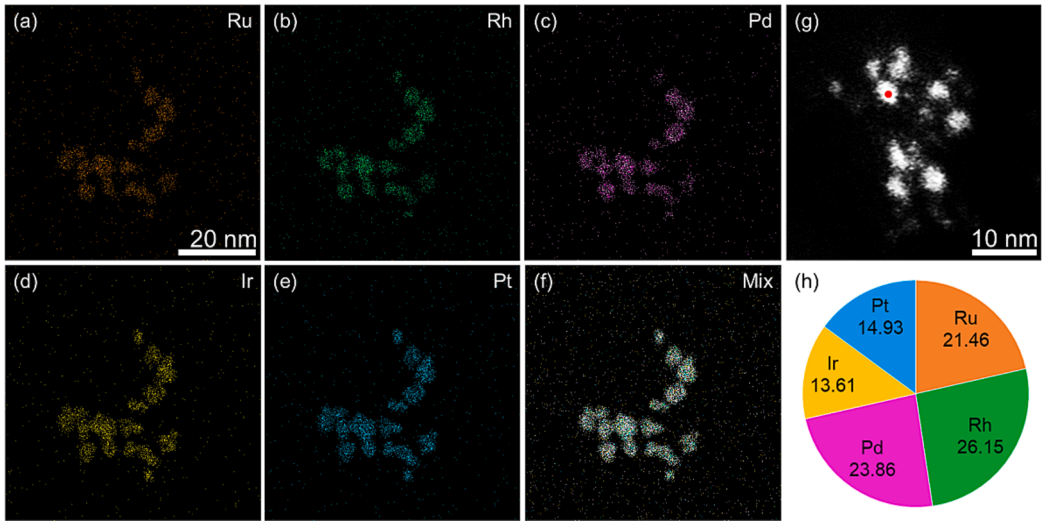

Fig. 3. STEM-EDX maps of 5PGM HEA NPs using (a) Ru-L, (b) Rh-L, (c) Pd-L, (d) Ir-L, and (e) Pt-L lines. (f) EDX map of mixture of all elements. (g) STEM-HAADF image of another 5PGM HEA NPs and (h) the composition ratio obtained using STEM-EDX point analysis. The analysis point is indicated by a red point in (g).

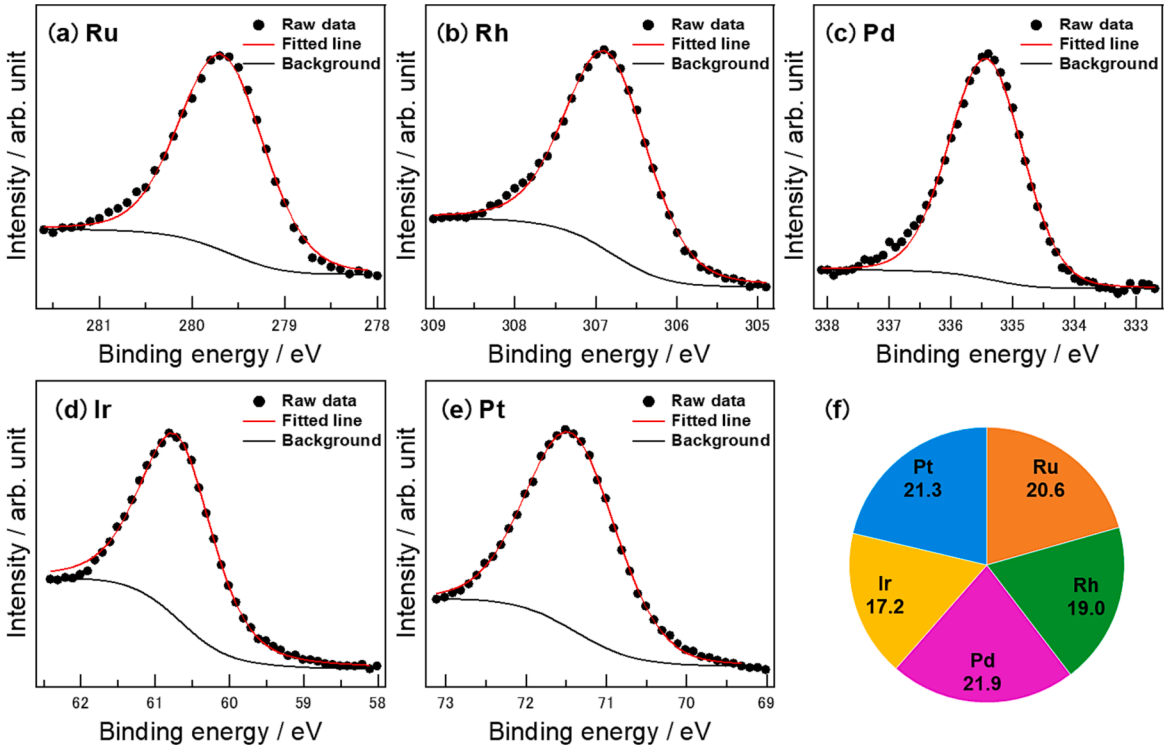

Fig. 4. XPS spectra of (a) Ru $3d_{5/2}$, (b) Rh $3d_{5/2}$, (c) Pd $3d_{5/2}$, (d) Ir $4f_{7/2}$, and (e) Pt $4f_{7/2}$ levels of 5PGM HEA NPs. (f) Compositions of 5PGM in HEA NPs obtained using XPS.

SWCNT growth to characterize their crystallinity. The XRD pattern of (1 1 1) diffraction peak and PDF of 5PGM HEA NPs after SWCNT growth are shown in Fig. 8 (a) and (b), respectively. For comparison, the XRD pattern and PDF of as-prepared 5PGM HEA NPs and those after heating at 750 ℃ for 3 min are also shown. Although the narrowing of (1 1 1) peak was seen after the heating, the diffraction angle of each (1 1 1) peak was the same (Fig. 8 (a)). In the PDF, 6 peaks corresponding to the atomic distances in the fcc structure of 5PGM HEA were seen, where there was no remarkable change in the distribution of distances between pairs of atoms even after the heating and SWCNT growth (Fig. 8 (b)). Furthermore, lattice fringes of the HRTEM image for 5PGM HEA NPs with a diameter of ~ 3 nm after SWCNT growth showed the same distance of (1 1 1) planes in the fcc structure (Fig. 8 (c)). These results indicate that both long-range order and local structure of 5PGM HEA NPs did not show a marked change during SWCNT growth, confirming their robustness.

3.3. Catalyst activity

To compare the activity of the 5PGM HEA NPs with that of monometallic catalysts, we performed SWCNT growth with Ru, Pd, Ir, and Pt catalysts on SiO_2/Si substrates by CVD using C_2H_2 as the feedstock gas. We also grew SWCNTs using extensively used-Fe and Co catalysts with Al_2O_3 support layers on Si substrates [24,25]. The optimal growth

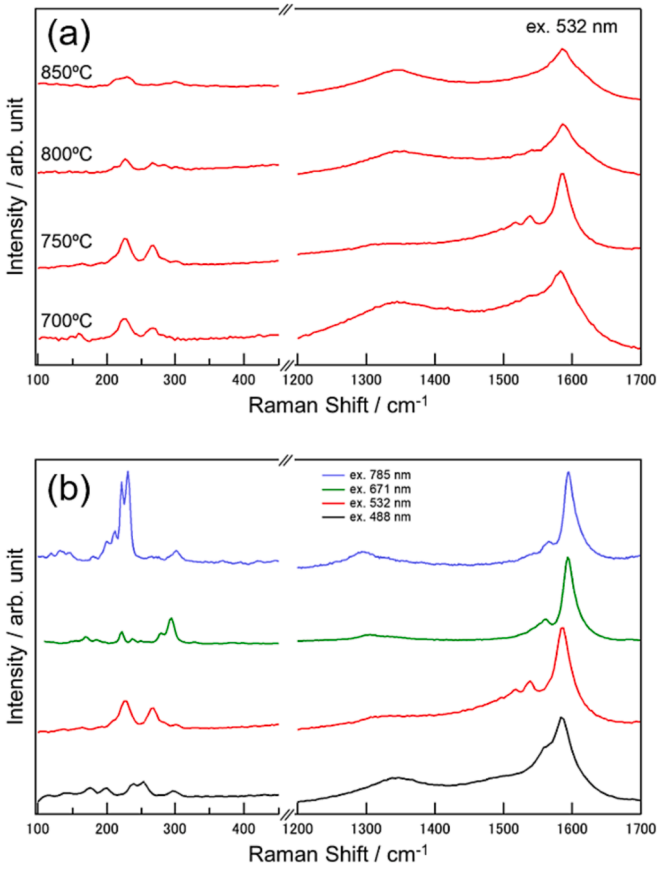

Fig. 5. (a) Raman spectra of SWCNTs grown at 700, 750, 800, and 850 ℃ by CVD with 5PGM HEA NP catalysts under the optimal Ar/C_2H_2 flow rate. The flow rate of Ar/C_2H_2 was optimized for each growth temperature (50, 300, 600, and 900 sccm for 700 ℃, 750 ℃, 800 ℃, and 850 ℃, respectively). The excitation wavelength is 532 nm. (b) Raman spectra of SWCNTs grown at 750 ℃ by CVD with 5PGM HEA NP catalysts. Raman spectra were measured using lasers with four excitation wavelengths (488, 532, 671, and 785 nm).

conditions for each catalyst were determined by performing SWCNT growth for 10 min at various growth temperatures and flow rates of Ar/C_2H_2. The Raman spectra of the samples grown under the optimal growth conditions showed that, except for Pd, both the RBM and G-band peaks appeared, indicating the growth of SWCNTs from the Ir, Pt, Ru, Fe, and Co catalysts (Fig. S4(a)–(e)). With an excitation wavelength of 671 nm, the G/D ratio of SWCNTs from 5PGM HEA NP catalysts was 10.7 (Fig. 5(b)), which was higher than those from the Ir, Pt, and Ru catalysts, and the value of G/D ratio was compatible for those from Fe and Co catalysts. This confirms that the quality of SWCNTs from 5PGM HEA NP catalysts were good. The SEM images showed that web-like SWCNTs were grown from the Ir, Pt, Ru, Fe, and Co catalysts (Fig. S5(a)–(e)). In the case of Pd, SWCNT growth could not be confirmed possibly (Fig. S5 (f)) because of both aggregation of Pd catalysts and their low activity for C_2H_2 [15]. Because the ratio of G-band peak intensity to the intensity of Si phonon peak at 520 cm^{-1} (G/Si ratio) is approximately proportional to the SWCNT yield [14–16], we calculated the G/Si ratio from the Raman spectra of SWCNTs grown from each catalyst to characterize the SWCNT yield (Fig. S6). In Fig. 9, the G/Si ratio for each catalyst is plotted as a vertical line in the logarithmic form. The G/Si ratio of SWCNTs grown with 5PGM HEA NPs is dependent on the detection area. This is because the homogeneity of 5PGM HEA NPs on the substrate prepared by the spin-coating method was worse than those of monometal catalyst particles and there would be the density distribution of the 5PGM HEA NPs. To avoid the influence of density distribution, we performed Raman measurements for 10 or more points on the substrates and plotted the average value with the error bar giving the information about the dispersion of G/Si ratio for each catalyst. The average G/Si ratios for SWCNTs grown with the Ru, Ir, and Pt catalysts are below 0.3, whereas that of the 5PGM HEA NPs is ~ 1.3. Irrespective of the in-plane distribution, the G/Si ratio of the SWCNTs grown with 5PGM HEA NPs was larger than those grown with Ru, Ir, and Pt catalysts, indicating that the SWCNT yield with 5PGM HEA NPs was much higher than that with PG monometal catalysts. Considering that the density of 5PGM HEA NPs on the substrate was lower than those of monometal platinum-group metal catalysts, as inferred from TEM and XPS results (Fig. 1, S2 and S3), this indicates that the catalyst activity of the 5PGM HEA NPs was higher than those of Pd, Ru, Ir, and Pt. We also evaluated the G/Si ratio of the SWCNTs grown with the Fe/Al_2O_3 and Co/Al_2O_3 catalysts under optimal growth conditions. The G/Si ratios of these catalysts were 1.6–2.4, which were much larger than those of the monometal PG catalysts. However, despite their high yields, the G/Si ratios of SWCNTs grown with the 5PGM HEA NP catalysts were compatible with those of the Fe and Co catalysts. Again, considering the lower density of 5PGM HEA NPs on the substrates, this substantiates the high catalytic activity of 5PGM HEA NPs for SWCNT growth.

In general, the d-band center of a transition metal is strongly related to its catalytic activity. As the d-band center approaches the Fermi level, the adsorption energy of the molecules generally increases. This implies that metal particles can catalyze a larger amount of feedstock gas, thereby acting as highly active catalysts [26]. Therefore, to investigate the relationship between the catalyst activity and the d-band center, we evaluated the d-band center of the 5PGM HEA NPs by performing an XPS analysis of the valence band. From the valence band spectra of each metal, we evaluated the d-band center relative to the Fermi level using Equation (1) [27]:

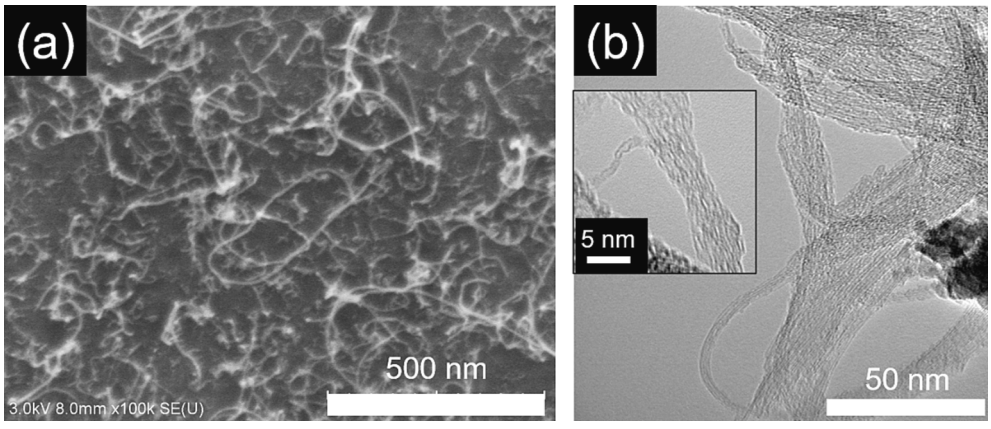

Fig. 6. (a) SEM and (b) TEM images of SWCNTs grown at 750 ℃ from 5PGM HEA NPs. The inset of (b) shows the high magnification image of SWCNTs.

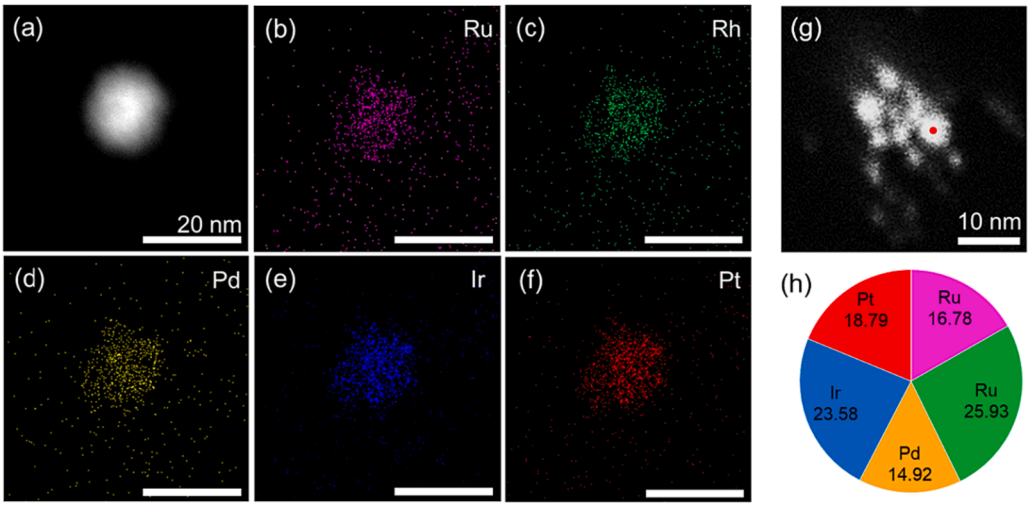

Fig. 7. (a) STEM-HAADF image of 5PGM HEA NPs after SWCNT growth. Corresponding STEM-EDX maps of (b) Ru-L, (c) Rh-L, (d) Pd-L, (e) Ir-L, and (f) Pt-L lines. (g) STEM-HAADF image of another 5PGM HEA NPs after SWCNT growth and (h) the composition ratio obtained using STEM-EDX point analysis. The analysis point is indicated by a red point in (g).

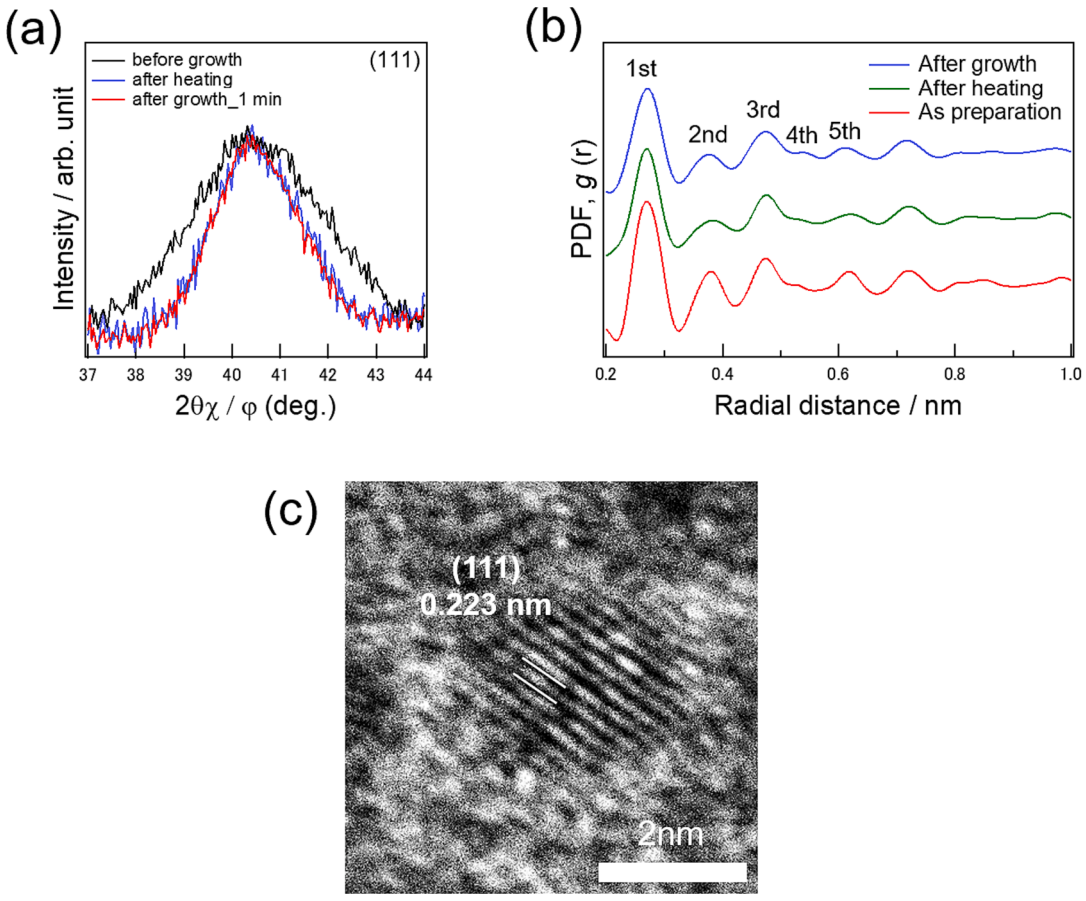

Fig. 8. (a) XRD pattern of (1 1 1) diffraction peaks and (b) pair distribution functions of as-prepared 5PGM HEA NPs, 5PGM HEA NPs after heating at 750 ℃ for 3 min and that after SWCNT growth. (c) High-resolution TEM image of 5PGM HEA NPs after SWCNT growth.

$$\text{d band center} = \frac{\int E \bullet DOS(E)dE}{\int DOS(E)dE} \quad (1)$$

where DOS(E) is the density of states of the occupied d states at binding energy E. Here, we assumed the valence band spectra obtained from the XPS analysis to be DOS(E), considering that the photoionization cross sections of the d states are much larger than those of the s and p states [28]. As reported previously [11], the valence band of HEA NPs shows a "featureless" spectrum (Fig. S7). For comparison, we also performed XPS measurements for Ru, Pd, Ir, Pt, Fe, and Co and evaluated the d-band center for each element. The relationship between the G/Si ratio and d-band center for each catalyst is shown in Fig. 9. The d-band centers of

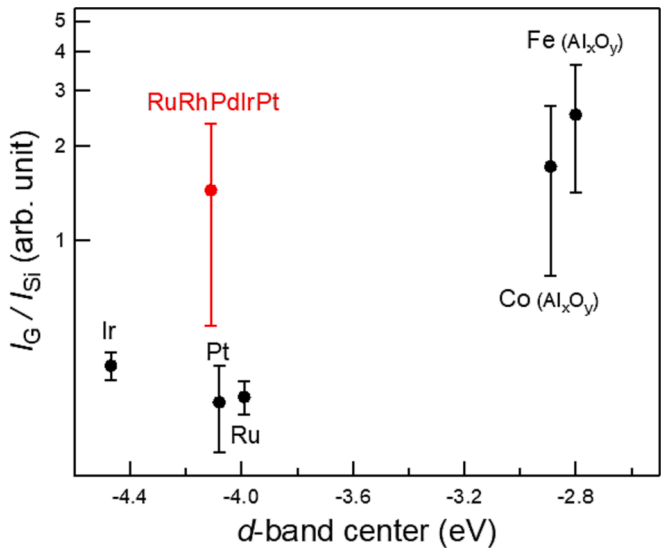

Fig. 9. Relationship between d-band centers of 5PGM HEA, Ru, Ir, Pt, Fe, and Co, and the G/Si ratio of SWCNTs grown with them as catalysts.

Ru, Pd, Ir, and Pt determined by XPS analysis are almost identical to those reported in a previous study [29]. For the monometallic catalysts, the G/Si ratio generally increased as the d-band center approached the Fermi level, as expected. In contrast, the d-band center of the 5PGM HEA NPs is located far from the Fermi level, although the G/Si ratio of the SWCNTs from the 5PGM HEA NP catalysts is high. This suggests that the HEA NPs behave quite differently from pure metal catalysts. This could be because HEA NPs have various surface sites, some of which would show high activity, as indicated in previous studies on HEA catalysts [10]. At present, identifying the active site for SWCNT growth is difficult because there are numerous sites on the surface of 5PGM HEA NPs. One of the candidates is the sites related to Pd atoms; among the PGM, Pd surface is known to be highly active in the cyclization reaction of acetylene to benzene [30,31], and Abbet et al. reported that even a single Pd atom catalyzes the production of benzene [32]. Such a catalytic property of Pd atom might play efficiently to obtain high-yield SWCNT. As shown in Fig. S5, SWCNTs were not grown from Pd catalysts because of the enlargement of particle sizes caused by aggregation [15]. Due to the stabilization by HEA, the enlargement of particle size was suppressed, as a result, the high catalytic activity of Pd atom in the cyclization reaction might be utilized to grow SWCNTs with high yield.

4. Conclusions

We succeeded in growing SWCNT by CVD using 5PGM HEA NP catalysts, which were solid solutions homogeneously composed of Ru, Rh, Pd, Ir, and Pt in almost equal atomic ratios. High-density SWCNTs were grown from 5PGM HEA NPs, most of whose lengths were longer than 1 μm. Raman analysis showed that SWCNTs grown from 5PGM HEA had diameters in the range of 0.83–1.1 nm, and the G/Si ratio was ~ 1.3, which was much higher than those of SWCNTs grown with monometal PGM catalysts. Furthermore, the G/Si ratio was comparable to that of SWCNTs grown using Fe and Co catalysts, which are the most common catalysts used to obtain high-yield SWCNTs. Our results show that, compared to monometal catalysts, 5PGM HEA NPs act as highly active catalysts for the growth of small-diameter SWCNTs. This could be due to the unique properties of HEA NPs, where various surface sites for the catalytic reaction are available because of the diversity of atomic configurations with specific local electronic structures.

CRediT authorship contribution statement

Shu Matsuoka: Writing – original draft, Methodology, Investigation, Formal analysis, Data curation, Conceptualization. **Kamal Prasad Sharma:** Validation, Methodology, Formal analysis. **Takahiro Saida:** Validation, Investigation. **Kohei Kusada:** Validation, Investigation. **Hiroshi Kitagawa:** Validation, Investigation. **Takahiro Maruyama:** Writing – review & editing, Supervision, Project administration, Funding acquisition, Conceptualization.

Declaration of competing interest

The authors declare that they have no known competing financial interests or personal relationships that could have appeared to influence the work reported in this paper.

Data availability

The data that has been used is confidential.

Acknowledgments

This study was supported by the Meijo University Nanomaterial Research Center and the Meijo University graduate students research grant A. STEM observations were performed at the Institute for Molecular Science (IMS) and the Nagoya Institute of Technology (NIT), supported by the Advanced Research Infrastructure for Materials and Nanotechnology in Japan (ARIM; JPMXP1223MS1018) of the Ministry of Education, Culture, Sports, Science, and Technology (MEXT), Japan. The authors thank Ms. S. Iki and Ms. K. Hirano at IMS for their support. We also thank Prof. T. Asaka at NIT for their support about characterization of catalyst particles by TEM.

Appendix A. Supplementary data

Supplementary data to this article can be found online at https://doi.org/10.1016/j.cplett.2024.141178.

References

[1] J. Yeh, S. Chen, J. Gan, T. Chin, T. Shun, C. Tsau, S. Chang, Formation of simple crystal structure in Cu-Co-Ni-Cr-Al-Fe-Ti-V-V alloys with multiprincipal metallic elements, Metall. Mater. Trans. A 35 (2004) 2533–2536.
[2] D. Miralcle, O. Senkov, A critical review of high entropy alloys and related concepts, Acta Mater. 122 (2017) 448–511.
[3] E. George, D. Raabe, R. Ritche, High-Entropy Alloys. Nat. Rev. Mater. 4 (2019) 515–534.
[4] L. Yu, K. Zeng, C. Li, X. Lin, H. Liu, W. Shi, H.-J. Qiu, Y. Yuan, Y. Yao, High-entropy alloy catalysts: from bulk to nano toward highly efficient carbon and nitrogen catalysis, Carbon Energy 4 (2022) 731–761.
[5] Y. Yao, Z. Huang, P. Xie, S.D. Lacey, R.J. Jacob, H. Xie, F. Chen, A. Nie, T. Pu, M. Rehwoldt, D. Yu, M.R. Zachariah, C. Wang, R. Shahbazian-Yassar, J. Li, L. Hu, Carbothermal shock synthesis of high-entropy-alloy nanoparticles, Science 359 (2018) 148–1494.
[6] Y. Yao, Z. Liu, P. Xie, H.Z. Huang, T. Li, D. Morris, Z. Finfrock, J. Zhou, M. Jiao, J. Gao, Y. Mao, J. Miao, P. Zhang, R. Shahzazian-Yassar, C. Wang, G. Wang, L. Hu, Computational aided, entropy-driven synthesis of highly efficient and durable multi-elemental alloy catalysts, Sci. Adv. 6 (2020) eaaz0510.
[7] T. Löffler, H. Meyer, A. Savan, P. Wilde, A.G. Manjón, Y.T. Chen, E. Ventosa, C. Scheu, A. Ludwig, W. Schuhmann, Discovery of a multinary Noble metal-free oxygen reduction catalyst, Adv. Energy Mater. 8 (2018) 1802259.
[8] K. Kusada, D. Wu, H. Kitagawa, New aspects of platinum group metal-based solid-solution alloy nanoparticles: binary to high-entropy alloys, Chem. Eur. J. 26 (2020) 5105–5130.
[9] K. Kusada, T. Yamamoto, T. Toriyama, S. Matsumura, K. Sato, K. Nagaoka, K. Terada, Y. Ikeda, Y. Hirai, H. Kitagawa, Nonequilibrium flow-synthesis of solid-solution alloy nanoparticles: from immiscible binary to high-entropy alloy, J. Phys. Chem. C 125 (2021) 458–463.
[10] D. Wu, K. Kusada, T. Yamamoto, T. Toriyama, S. Matsumura, S. Kawaguchi, Y. Kubota, H. Kitagawa, Platinum-group-metal high-entropy-alloy nanoparticles, J. Am. Chem. Soc. 142 (2020) 13833–13838.
[11] D. Wu, K. Kusada, Y. Nanba, M. Koyama, T. Yamamoto, T. Toriyama, S. Matsumura, O. Seo, I. Gueye, J. Kim, L. Singgapulige, R. Kumara, O. Sakata, S. Kawaguchi, Y. Kubota, H. Kitagawa, Noble-metal high-engropy-alloy

nanoparticles: atomic-level insight into the electronic structure, J. Am. Chem. Soc. 144 (2022) 3365–3369.
[12] H. Minamihara, K. Kusada, D. Wu, T. Yamamoto, T. Toriyama, S. Matsumura, L.S. R. Kumara, K. Ohara, O. Sakata, S. Kawaguchi, Y. Kubota, H. Kitagawa, Continuous-flow reactor synthesis for homogeneous 1 nm-sized extremely small high-entropy alloy nanoparticles, J. Am. Chem. Soc. 144 (2022) 11525–11529.
[13] H. Minamihara, K. Kusada, T. Yamamoto, T. Toriyama, Y. Murakami, S. Matsumura, L.S.R. Kumara, O. Sakata, S. Kawaguchi, Y. Kubota, O. Seo, S. Yasuno, H. Kitagawa, J. Am. Chem. Soc. 145 (2023) 17136–17142.
[14] T. Maruyama, H. Kondo, R. Ghosh, A. Kozawa, S. Naritsuka, Y. Iizumi, T. Okazaki, S. Iijima, Single-walled carbon nanotube synthesis using pt catalysts under low ethanol pressure via cold-wall chemical vapor deposition in high vacuum, Carbon 96 (2016) 6–13.
[15] H. Kiribayashi, S. Ogawa, A. Kozawa, T. Saida, S. Naritsuka, T. Maruyama, Low-temperature growth of single-walled carbon nanotubes using Al_2O_3/Pd/Al_2O_3 multilayer catalyst by alcohol gas source method at high vacuum, Jpn. J. Appl. Phys. 55 (2016) 06GF04.
[16] T. Maruyama, A. Kozawa, T. Saida, S. Naritsuka, S. Iijima, Low temperature growth of single-walled carbon nanotubes from rh catalysts, Carbon 116 (2017) 128–132.
[17] T. Fujii, H. Kiribayashi, T. Saida, S. Naritsuka, T. Maruyama, Low temperature growth of single-walled carbon nanotubes from ru catalysts by alcohol catalytic chemical vapor deposition, Diamond Relat. Mater. 77 (2017) 97–101.
[18] T. Maruyama, T. Okada, K.P. Sharma, T. Suzuki, T. Saida, S. Naritsuka, Y. Iizum, T. Okada, S. Iijima, Vertically aligned growth of small-diameter single-walled carbon nanotubes by alcohol catalytic chemical vapor deposition with ir catalyst, Appl. Surf. Sci. 509 (2020) 145340.
[19] A. Misaki, T. Saida, S. Naritsuka, T. Maruyama, Effect of growth temperature and ethanol flow rate on synthesis of single-walled carbon nanotube by alcohol catalytic chemical vapor deposition using ir catalyst in hot-wall reactor, Jpn. J. Appl. Phys. 60 (2021) 015003.
[20] T. Maruyama, D. Yamamoto, M. Kobayashi, K.P. Sharma, T. Saida, S. Naritsuka, Osumium catalyzed growth of vertically aligned and small-diameter single-walled carbon nanotubes by alcohol catalytic chemical vapor deposition, Diamond Relat. Mater. 117 (2021) 108501.
[21] S.D.M. Brown, A. Jorio, M.S. Dresselhaus, G. Dresselhaus, Observation of the D-band feature in the raman spectra of carbon nanotubes, Phys. Rev. B 64 (2001) 073403.
[22] A. Jorio, R. Saito, J.H. Hafner, C.M. Liever, M. Hunter, T. McClure, G. Dresselhaus, M.S. Dresselhaus, Structural (n, m) determination of isolated Single-Wall carbon nanotubes by resonant raman scattering, Phys. Rev. Lett. 86 (2001) 1118.
[23] V. Jourdain, C. Bichara, Current understanding of the growth of carbon nanotubes in catalytic chemical vapour deposition, Carbon 58 (2013) 2–39.
[24] K. Hata, D.N. Futaba, K. Mizuno, T. Namai, M. Yumura, S. Iijima, Water-assisted highly efficient synthesis of impurity-free single-walled carbon nanotubes, Science 306 (2004) 1362–1364.
[25] A. Kaneko, K. Yamada, R. Kumahara, H. Kato, Y. Homma, Comparative study of catalytic activity of iron and cobalt for growing carbon nanotubes on alumina and silicon oxide, J. Phys. Chem. C 116 (2012) 26060–260656.
[26] J.K. Nørskov, F. Abild-Pedersen, F. Studt, T. Bligaard, Density functional theory in surface chemistry and catalysis, PNAS 108 (2011) 937–943.
[27] A. Vojvodic, J.K. Nørskov, F. Abild-Pedersen, Electronic structure effects in transition metal surface chemistry, Top Catal. 57 (2014) 25–32.
[28] J.J. Yeh, I. Lindau, Atomic subshell photoionization cross sections and asymmetry parameters: $1 \leq Z \leq 103$. academic press, Inc. Atomic Data and Nuclear Data Tables 32 (1985).
[29] D. Wu, K. Kusada, T. Yamamoto, T. Toriyama, S. Matsumura, I. Guey, O. Seo, J. Kim, S. Hiroi, O. Sakata, Y. Kubota, H. Kitagawa, Correction: on the electronic structure and hydrogen evolution reaction activity of platinum group metal-based high-enetropy-alloy nanoparticles, Chem. Sci. 12 (2021) 7196.
[30] W.T. Tysoe, G.L. Nyberg, R.M. Lambert, Photoelectron spectroscopy and heterogeneous catalysis: benzene and ethylene from acetylene on palladium (111), Surf. Sci. 135 (1983) 128.
[31] T.G. Rucker, M.A. Logan, T.M. Gentle, E.L. Muetterties, G.A. Somorjai, Conversion of acetylene to benzene over palladium single-crystal surfaces. 1. the low-pressure stoichiometric and the high-pressure catalytic reactions, J. Phys. Chem. 90 (1986) 2703–2708.
[32] S. Abbet, A. Sanchez, U. Heiz, W.D. Schneider, A.M. Ferrari, G. Pacchioni, N. Rösch, Acetylene cyclotrimerization on supported size-selected pdn clusters ($1 \leq n \leq 30$): one atom is enough!, J. Am. Chem. Soc. 122 (2000) 3453–3457.